Journal of
Marine Science and Engineering

MDPI

Article

Seagrass Resource Assessment Using WorldView-2 Imagery in the Redfish Bay, Texas

Lihong Su [1,*] and Yuxia Huang [2]

[1] Harte Research Institute for Gulf of Mexico Studies, Texas A&M University-Corpus Christi, 6300 Ocean Drive, Unit 5869, Corpus Christi, TX 78412, USA
[2] Department of Computing Sciences, Texas A&M University-Corpus Christi, 6300 Ocean Drive, Unit 5824, Corpus Christi, TX 78412, USA; lucy.huang@tamucc.edu
* Correspondence: su.lihong@tamucc.edu; Tel.: +1-361-825-2069

Received: 25 March 2019; Accepted: 4 April 2019; Published: 10 April 2019

Abstract: Seagrass meadows play important roles as habitats for many marine organisms, traps for sediment, and buffers against wave actions. The objective of this paper is to map seagrass meadows in the Redfish Bay, Texas from WorldView-2 imagery. Seagrass meadows grow in shallow and clear water areas in the Redfish Bay. The WorldView-2 satellite can acquire multispectral imagery from the bay bottom with 2 m spatial resolution 8 multispectral bands and 0.46 m panchromatic imagery. The top of atmosphere radiance was transformed to the bottom reflectance through the atmospheric correction and the water column correction. The object based image analysis was used to identify seagrass meadows distributions in the Redfish Bay. This investigation demonstrated that seagrass can be identified with 94% accuracy, although seagrass species cannot be satisfactorily recognized. The results implied that the WorldView-2 satellite imagery is a suitable data source for seagrass distribution mapping.

Keywords: coastal water; water depth correction; seagrass; object-based image analysis; WorldView-2

1. Introduction

Submerged aquatic vegetation habitats such as seagrass communities are among the most productive coastal habitats and are vital to estuarine ecosystems. Seagrasses form extensive meadows in shallow coastal environments, where they provide a number of critical ecosystem services, including sediment stabilization and shoreline protection, maintaining water quality, and providing food and habitat for fish and other fauna [1–3]. The contribution of seagrass meadows-based ecosystems to the global ocean is disproportionate to their small areas [4]. However, distribution and growth of seagrass communities are adversely affected by direct human activities, such as eutrophication and physical damage from boating and fishing, as well as by indirect human impacts stemming from climate change, such as sea level rise [2]. Inventory and monitoring are critical components in seagrass ecosystem management, restoration and protection, and provide key insights into the overall health of estuarine ecosystems.

Traditional methods of quantifying seagrass distribution and growth involve individually counting, collecting and measuring seagrass as well as tagging seagrass blades for growth rate estimate. Although these direct observations can provide very accurate data, they are very time consuming and difficult to update large-scale quantitative maps [5]. Remote sensing presents feasible way for monitoring shallow coastal ecosystems with clear water due to good light penetration. Moreover, remote sensing has shown to be more cost-effective than field survey in some situations and should be used as an integral approach along with field survey for monitoring seagrass communities. Both satellite and airborne images have been used to investigate the seagrass meadows

distributed across the shallow waters. Some instances are medium spatial resolution data [6–8], aerial hyperspectral scanners [9–11], high spatial resolution imagery [12–16], and photos acquired by a lightweight drone [17]. Various techniques and input features were used in seagrass mapping. Obviously, the investigators selected suitable classifiers and input features for their seagrass mapping. Some investigators used pixel-based classifiers, for examples, the maximum likelihood classifier on the original spectral bands and the spectral indices [14], support vector machines on three sunglint-corrected spectral bands and a depth invariant index [8], classification trees on spectral index after simple atmospheric correction [18]. Some researchers mapped seagrass species by pixels using a physics based model inversion [19], or spectrum matching and look-up tables [10]. Other investigators used the object based image analysis (OBIA) with unsupervised classifier [17] or regression tree classifier [13]. Some researchers mapped seagrass by new computing platforms such as the cloud computing of Google Earth Engine [8].

Hossain et al. [20] comprehensively evaluated various methods employed to produce seagrass habitat maps using optical remote sensing during the past four decades. Based on 192 papers, Hossain et al. summarized that no single technology or approach is suitable for and capable of measuring all seagrass parameters (presence/absence, cover, species, and biomass) and assessing their change. Further research is required for to better understand theoretical and methodological aspects of seagrass remote sensing.

The seagrass meadows in the Texas Coastal Bend usually grow in relatively narrow shallow (less than 1.5 m deep) and clear water areas along the bay shores [21]. This situation requires high spatial resolution imagery, such as aerial photography and high spatial resolution multispectral satellite imagery. WorldView-2 satellite could be a suitable data source, as it can acquire imagery from the bay bottom in clear water with 2 m spatial resolution. The OBIA is an effective approach of extracting features from the high spatial resolution imagery [22,23]. The objective of this paper is to mapping seagrass meadows in the Redfish Bay from WorldView-2 high spatial resolution imagery with the OBIA method. To obtain accurate reflectance of the seabed for facilitating the classification, we also present an approach of water column correction in this paper.

2. Experiment Site and Satellite Data

The study area (Figure 1) is the Redfish Bay (27.9078° N and 97.11277° W), where has an average depth of 0.75 m and a maximum depth of about 2 m, a major component of the Mission-Aransas National Estuarine Research Reserve [24], at Texas coast. The Redfish Bay has a semiarid and subtropical climate [25]. On average, the coolest month is January with average low 11 °C and high 17 °C; the warmest month is August with average low 27 °C and high 32 °C. Mean annual precipitation is around 915 mm and the most rainfall on average occurs in September. *Halodule wrightii* and *Thalassia testudinum* are co-dominant seagrass species [26] in this shallow estuarine ecosystem. Seagrasses commonly flourish as meadows in soft sediments at and below the intertidal zone in shallow water less than 1.5 m deep [27]. The Redfish Bay is characterized by high nutrient levels and is influenced by fairly turbid waters [28]. Elevated nutrient and chlorophyll *a* levels usually lead to abundant phytoplankton in the water column, which indicates low water transparency. High total suspended sediments, particularly sediments re-suspended by winds and waves, contribute to turbidity of the water in this shallow bay as well. The Redfish Bay is also reported to have low levels of dissolved oxygen and high epiphytic growth [28]. The low water transparency reduces the amount of light reaching seagrass leaves. When silt or phytoplankton settle on seagrass leaves, the amount of light reaching the leaves will be further reduced. Reduced water quality not only reduces the distribution of seagrass from deeper water [29,30], but also increases the need for water column correction of remotely-sensed spectral signals.

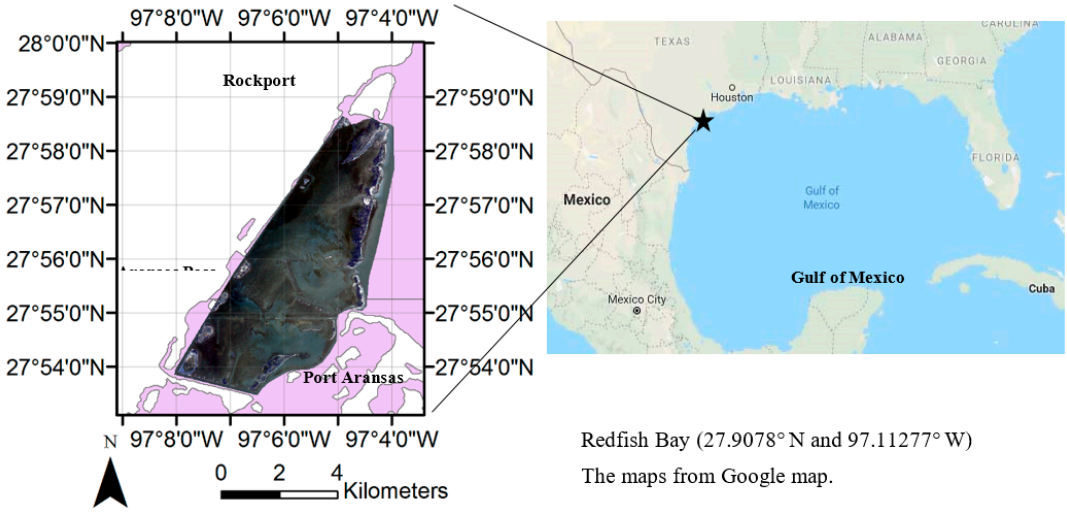

Figure 1. Location of the study site.

A cloud free WorldView-2 image acquired at 17:13 p.m. on 16 December 2010 was used in the seagrass mapping. The sun zenith angle was 53°, the satellite zenith angle was 32°, the relative azimuth angle was 103°. The top-of-atmosphere radiance image of the WorldView-2 scene was produced through the radiometrical correction and the sensor correction. The radiance image was then projected to UTM North Zone 14 on WGS84. After that, an image registration was conducted. The position accuracy of this scene is better than 1 pixel comparing with GPS positions.

3. Methods for Data PROCESSING and Classification

The WorldView 2 image was processed from raw data to bottom reflectance by our C# program, and then the classification was carried out on the bottom reflectance data by ENVI. The workflow of processing and classification is shown in Figure 2.

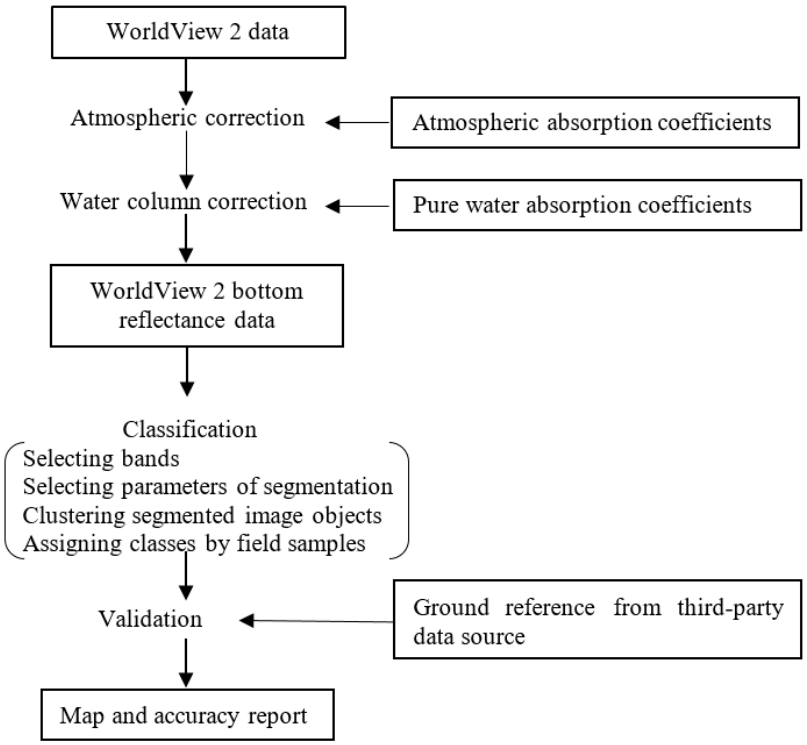

Figure 2. The workflow of the data processing and classification.

3.1. Satellite Data Processing for Bottom Reflectance

Creating accurate seagrass maps is a challenging procedure in coastal waters with variable atmospheric condition and water clarity and depths. The aquatic plants information in shallow waters can be retrieved from optical remote sensing images by following the fundamental physical principle. Here, light becomes attenuated by interaction with the water column when downwelling light passes through water. The downwelling light reflected from the bottom to generate upwelling light. The upwelling light is absorbed in the passage through the water column before the light leaves water surface.

The total upwelling radiance (L_t) recorded by the remote sensor consists of four components [31,32]: bottom radiance (L_b), subsurface volumetric radiance (L_v), specular radiance (L_s), and atmospheric path radiance (L_p) as shown in Equation (1):

$$L_t = L_b + L_v + L_s + L_p \quad (1)$$

Atmospheric path radiance (L_p) is a function of atmospheric scattering, including both Rayleigh (molecular) scattering and Mie (aerosol) scattering. Subsurface volumetric radiance (L_v) results from volume scattering from the water and its organic/inorganic constituents (e.g., sediment and chlorophyll). Specular radiance (L_s) is the reflection from the water surface, including possible sun glint effects. The bottom radiance (L_b) is the energy reflected from the seabed, which integrates the information about water depth and bottom characteristics (habitat and substrate). To obtain seabed information, we need to disaggregate bottom radiance (L_b) from total radiance (L_t). This paper proposed a bio-optical approach to remove L_v from L_t as detailed in Section 3.1.4.

3.1.1. Land and Cloud Masking

When extracting aquatic information, it is necessary to eliminate all upland and terrestrial features [33]; thus all upland features, as well as boats, piers, and clouds were masked out of all the images. The "land-mask" restricts the spectral range of radiance values to aquatic features and allows for detailed feature discrimination. In this paper, radiance values of the near infrared (NIR) band were used to prepare the binary mask that was subsequently applied to all the channels.

3.1.2. Sun Glint Correction

An extensive review on the sun glint correction was given by Kay et al. [34]. Several algorithms were proposed for shallow water areas of high spatial resolution multispectral satellite image [35–37]. The most straightforward way to deal with the sun glint problem is to avoid it by an appropriate choice of place and time for image acquisition [34]. Numerical simulation of radiative transfer conducted by Mobley [38] suggest that a viewing angle of 40° from nadir and 135° from the sun is optimal for avoiding glint. Fortunately, the WorldView-2 image used in this study was acquired with a good chance to avoid the sun glint by viewing angle of 32° from nadir and 103° from the sun. Visible inspection also shows that this image had no significant sun glint effects. Specifically, there are no significant bright and dark portions on the image, therefore no sun glint correction was needed here.

3.1.3. Atmospheric Correction

The atmospheric correction was used to correct atmospheric effects on the total upwelling radiance L_t. For the high visibility condition, we ignored any Rayleigh-aerosol multiple scattering. Using the algorithm developed by Stumpf [39,40], the atmospheric diffuse transmission coefficient and the Rayleigh path radiance were computed and applied to the WorldView-2 image. The Rayleigh scattering coefficient is wavelength-dependent. The coefficients were calculated using the equations developed by Evans and Gordon [41]. Ozone absorption coefficient was calculated using data collected by Elterman [42]. The coefficients for the WorldView-2 are displayed on Table 1. Here, $\tau_R(\lambda)$ is the Rayleigh optical thickness. $\tau_{Oz}(\lambda)$ is the Ozone optical thickness. ESun is the WorldView-2

band-averaged solar spectral irradiance ($\mu Wcm^{-2}nm^{-1}$) [43]. $T_2(\lambda)$ is the atmospheric diffuse transmission coefficient. $L_{PR}(\lambda)$ is the Rayleigh path radiance ($\mu Wcm^{-2}nm^{-1}$). *Corr* is the correct coefficient integrating earth-sun distance, in-band solar irradiance, solar zenith angle and π. The aerosol scattering for the scene was derived by subtracting the Rayleigh path radiance from top of atmosphere (TOA) radiance in clear deep water pixels of the NIR band. The NIR channel is used for this correction because there is practically no water volume scattering or bottom-reflected signal in this channel. The correction can be applied over the entire scene without changing the depth dependence of the corrected signal [44].

Table 1. Coefficients for atmospheric correction of the WorldView-2 scene ($\tau_R(\lambda)$ is the Rayleigh optical thickness. $\tau_{Oz}(\lambda)$ is the Ozone optical thickness. ESun is the WorldView-2 band-averaged solar spectral irradiance ($\mu Wcm^{-2}nm^{-1}$). $T_2(\lambda)$ is the atmospheric diffuse transmission coefficient. $L_{PR}(\lambda)$ is the Rayleigh path radiance ($\mu Wcm^{-2}nm^{-1}$). *Corr* is the correct coefficient integrating earth-sun distance, in-band solar irradiance, solar zenith angle and π).

λ (nm)	$\tau_R(\lambda)$	$\tau_{Oz}(\lambda)$	ESun	*corr*	$T_2(\lambda)$	$L_{PR}(\lambda)$
427.3 Coastal	0.2845	0.0028	175.8223	0.020755	0.662284	6.277835
477.9 Blue	0.1795	0.0085	197.4242	0.018484	0.756456	4.376088
546.2 Green	0.1039	0.0295	185.641	0.019657	0.793434	2.243893
607.8 Yellow	0.0673	0.0042	173.8479	0.02099	0.898054	1.462551
658.8 Red	0.0485	0.0018	155.9456	0.0234	0.928669	0.951924
723.7 Red Edge	0.0332	0.0058	134.207	0.02719	0.938348	0.554454
831.3 NIR 1	0.0189	0.0020	106.973	0.034113	0.967996	0.254318
908.0 NIR 2	0.0133	0.0000	86.12866	0.042369	0.981286	0.144913

3.1.4. Water Column Correction

The atmosphere corrected image still contains information about water depth, water column constituents and the reflectance properties of substrate cover types [12,15,37,40,44–50]. Some studies did not conduct water column correction in their seagrass mapping for various data sources such as RGB photos by lightweight drone Duffy et al. [17], airborne color infrared imagery [13], airborne hyperspectral data [11], and high spatial resolution satellite imagery [14]. Actually Duffy et al. [17], Green and Lopez [13] did not conduct atmospheric correction neither. To reduce water column effects, this paper conducted water column correction based on radiative transferring in water.

In coastal waters, three major optical constituents cause wavelength dependent attenuation of light: chromophoric dissolved organic material (CDOM), phytoplankton photosynthetic pigment chlorophyll-a (Chl-a), and total suspended matter (TSM), which can be separated in organic and inorganic fractions. Generally, CDOM and Chl-a reduce the reflectance signal by absorbing light in the blue and red (Chl-a only) spectral ranges, while TSM increases the reflectance signal in the red region and shifts the green peak to longer wavelengths [31,51–53]. The apparent optical properties of water such as absorption (a) and backscattering coefficient (b_b) are the main physical agents governing the magnitude and spectral composition of the backscattered flux from the ocean surface [53–55].

The remote sensing reflectance of waters usually is defined by two forms: measurements above water surface or measurements just below water surface. Generally, R_{rs} is defined as a ratio of the upwelling radiance $L_w(0^+)$ to downwelling irradiance $E_d(0^+)$ just above water surface. r_{rs} is defined as a ratio of the upwelling radiance $L_w(0^-)$ to downwelling irradiance $E_d(0^-)$ just below water surface. The R_{rs} at every pixel of an image is produced by correcting the atmospheric effects on the top-of-atmosphere radiance image. The unit of both R_{rs} and r_{rs} is sr^{-1}. Due to the refractive effects of the water surface, R_{rs} is not equal to r_{rs}. Their relationship can be described by Equation (2) with accuracy within a few percent as explained by Mobley [38] and Lee et al. [56].

$$r_{rs} = \frac{R_{rs}}{0.52 + 1.7R_{rs}} \quad (2)$$

$$r_{rs} = r_{rs}^{dp}(1 - e^{-(D_0 + 1.03\sqrt{1+2.4u})kH}) + \frac{\rho}{\pi}e^{-(D_0 + 1.04\sqrt{1+5.4u})kH} \quad (3)$$

$$r_{rs}^{dp} = -0.00042 + 0.112\frac{b_b}{a} - 0.0455\left(\frac{b_b}{a}\right)^2 \quad (4)$$

$$a(\lambda) = M(\lambda)[a(490) - a_w(490)] + a_w(\lambda) \quad (5)$$

$$a(490) = \frac{a(440) + a_w(440)}{M(440)} + a_w(490) \quad (6)$$

$$a(440) = 10^{-0.619 - 1.969(\log_{10}(\frac{R_{rs}(490)}{R_{rs}(555)})) + 0.790(\log_{10}(\frac{R_{rs}(490)}{R_{rs}(555)}))^2} \quad (7)$$

$$b_b(\lambda) = b_{bp}(\lambda) + b_{bw}(\lambda) \quad (8)$$

$$b_{bp}(\lambda) = b_{bp}(440)\left(\frac{440}{\lambda}\right)^{\eta} \quad (9)$$

$$\eta = 2.2\left(1 - 1.2e^{(-0.9r_{rs}(440)/r_{rs}(555))}\right) \quad (10)$$

$$b_{bp}(440) = \frac{a_w(440)}{0.09}R_{rs}(440) \quad (11)$$

For optically shallow waters, r_{rs} can be approximated as a sum of contributions from the water column and from bottom by Equation (3) [56,57]. r_{rs}^{dp} is the reflectance r_{rs} for optically-deep waters (Equation (4)). a is the total absorption coefficient in m^{-1}. b_b is the backscattering coefficient in m^{-1}. $D_0 = 1/\cos(\theta_w)$ with θ_w the subsurface solar zenith angle. $k = a + b_b$. $u = b_b/(a + b_b)$. H is the depth of water in m. ρ is the bottom albedo, here we assume that seagrasses and soil are diffuse. The total absorption coefficient $a(\lambda)$ can be estimated by Eqution (5) [58,59]. M is statistically derived coefficients [58]. $a(490)$ is the total absorption coefficient at 490 nm. $a_w(490)$ is the pure-water absorption coefficient at 490 nm. The laboratory measured values of pure-water absorption coefficient by Pope and Fry [60] are widely accepted and used by ocean-optics community. We can thus rewrite Equation (5) to compute the total absorption coefficient at 490 nm by Equation (6). $M(440) = 1.5087$, derived with the equations established by Austin and Petzold [58]. According to Lee et al. [61], the total absorption coefficient at 440 nm over optically-deep water, can be empirically determined by Equation (7). $R_{rs}(490)$ and $R_{rs}(555)$ are remote sensing reflectance R_{rs} at 490 and 555 nm over the optically-deep water.

The backscattering coefficient $b_b(\lambda)$ may be expressed with Equation (8) [62,63]. $b_{bp}(\lambda)$ is the backscattering by particles in m^{-1}. $b_{bw}(\lambda)$ is the backscattering by water molecules in m^{-1}. The laboratory measured values of b_{bw} by Smith and Baker [63] are used here. $b_{bp}(\lambda)$ at wavelength λ can be estimated by $b_{bp}(440)$ with Equation (9) [63–65]. The power parameter η can be estimated from Equation (10) [66]. $r_{rs}(440)$ and $r_{rs}(555)$ can be calculated by using Equation (2) with R_{rs} at 490 and 555 nm. For optically-deep water, the backscattering coefficients by particles $b_{bp}(440)$ can be expressed as Equation (11) [67]. a_w is pure-water absorption coefficient of water.

It is noteworthy that the models to derive absorption and backscattering coefficients discussed above use wavelengths such as 440, 490 and 555 nm, applied to WorldView-2 coastal, blue and green bands, respectively. The deep water pixels are defined as those having very little upwelling signal in the visible bands of the dataset and are not affected by bottom albedo. We identified five polygons as the optically-deep water on the WorldView-2 image. The five sites and their mean of R_{rs} at six bands, namely Coastal, Blue, Green, Yellow, Red, and Red Edge, are displayed in Figure 3. The Secchi disk visibility was 2.1 m at Region of Interest 3, which was on the Gulf Intracoastal Waterway. The waterway has a controlling depth of 3.7 m, designed primarily for barge transportation. The spectrum are corresponding to the typical coastal water with chlorophyll and CDOM [52].

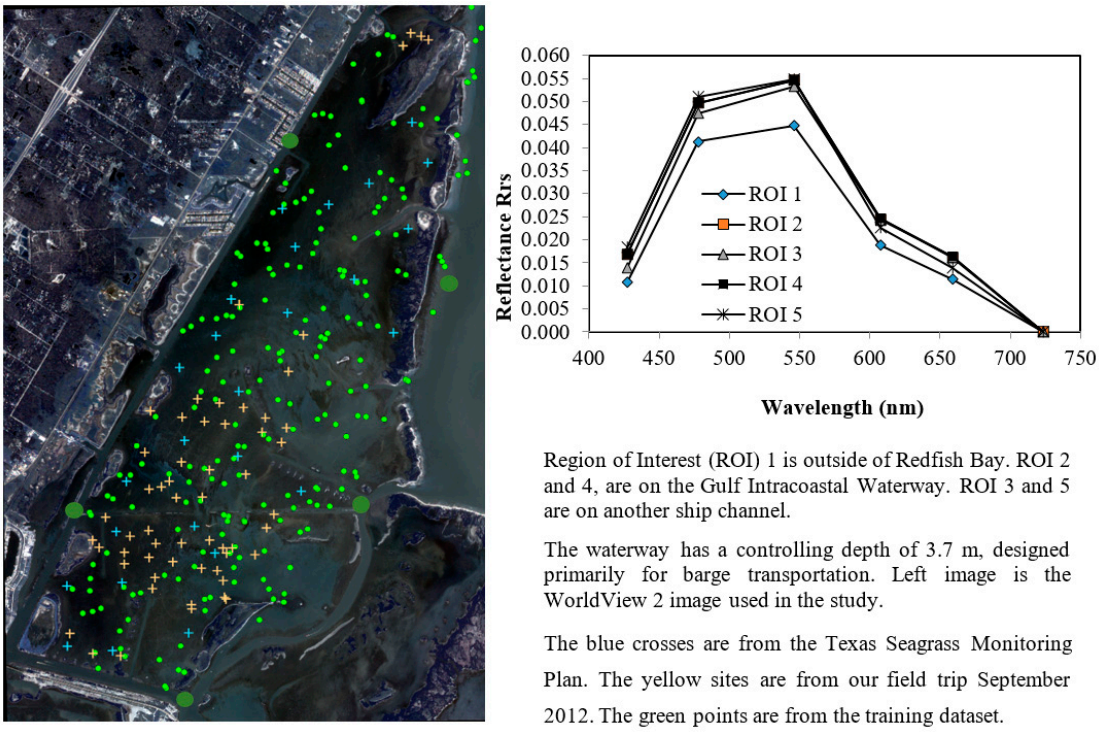

Figure 3. The validation data and five deep water sites and their spectrum.

Based on the average R_{rs} derived from the all pixels of the five deep water polygons, the $a(\lambda)$ and $b_b(\lambda)$ at the six bands are calculated by using Equations (5)–(11), and displayed on Table 2. Table 2 also shows Pope and Fry's $a_w(\lambda)$, Smith and Baker's $b_{bw}(\lambda)$, and Austin and Petzold's $M(\lambda)$. The water depth, H, was generated by the inverse distance weighted interpolation of the field survey data [68]. The error of interpolation was within 10 cm. The water column correction was carried out with the $a(\lambda)$, $b_b(\lambda)$ and H. The r_{rs} at every pixel is calculated by using Equation (2) from water-leaving reflectance R_{rs}. Finally the bottom albedo ρ is calculated by using Equations (3) and (4). The following classification was carried on the bottom ρ image.

Table 2. Coefficients for water column correction ($a_w(\lambda)$ and $b_{bw}(\lambda)$ are pure-water absorption and backscattering coefficients. $M(\lambda)$ is the coefficient defined by Austin and Petzold. a (λ) is the total absorption coefficient. $b_b(\lambda)$ is the backscattering coefficient).

Λ (nm)	$a_w(\lambda)$ (m^{-1})	$b_{bw}(\lambda)$ (m^{-1})	$M(\lambda)$	$a(\lambda)$ (m^{-1})	$b_b(\lambda)$ (m^{-1})
427.3 Coastal	0.0048	0.0043	1.5849	0.2984	0.0065
477.9 Blue	0.0121	0.0027	1.1055	0.2169	0.0047
546.2 Green	0.0511	0.0015	0.6174	0.1655	0.0034
607.8 Yellow	0.2629	0.0010	0.5130	0.3579	0.0027
658.8 Red	0.3930	0.0007	0.6797	0.5189	0.0023
723.7 Red Edge	1.7500	0.0005	0.1449	1.7768	0.0021

3.2. Classification and Accuracy Assessment

This study used OBIA to map seagrass. OBIA uses both spectral and spatial features, namely color, shape, size, texture and pattern, to group pixels into segments namely image objects based on the criteria of homogeneity. The segments have additional spectral information compared to single pixels (e.g., mean values per band, median values, minimum and maximum values, variance etc.), and are spatially contiguous, disjoint, and homogeneous. Although the OBIA has some disadvantages, such as the empirical selecting segmentation parameters and necessary knowledge of the characteristics of different ground objects, the OBIA technique is reportedly effective and superior compared to

the traditional pixel-based methods on high spatial resolution imagery. OBIA consists of two steps: (1) the image is delineated into segments and (2) The segments are classified to geographic objects. Technically, OBIA can use any of supervised or unsupervised classification methods to label the segments to geographic objects.

3.2.1. Band Selection

WorldView-2 imagery has eight bands in visible and near infrared spectrum. Except for the two NIR bands, the other six bands (Coastal, Blue, Green, Yellow, Red, and Red Edge) could be used to mapping seagrass. Suitable bands were selected by empirically and visually comparison of unsupervised classification results produced with the Iterative Self-Organizing Data Analysis Techniques (ISODATA) algorithm on various combinations of bands. The experiments show that Red Edge does not contribute significantly the clustering when it was added on Blue, Green and Red. It is understandable because water column attenuation at Red Edge is much stronger than other bands at short wavelength. The water column correction may bring more noise at Red Edge due to heavier correction. The experiments also show that Coastal and Blue together do not bring more information than either Coastal or Blue into the classification. With this regards, the four bands, Blue, Green, Yellow and Red, were selected for the seagrass mapping.

3.2.2. Method and Parameters Selection of Segmentation

We tried three software for segmentation: ENVI Feature Extraction, eCognition, and MatLab. Finally, we selected ENVI Feature Extraction in this study due to its ease of use. Its edge-based method with Full Lambda Schedule was used to produce the segments. This approach needs to set three parameters: Scale Level, Merge Level and Texture Kernel Size. Scale Level can be set from 0 to 100. Increasing its value results in fewer segments. Merge Level also can be set from 0 to 100. Increasing its value results in merging more segments. No merging occurs for the value of 0. Texture Kernel Size needs a value of odd number between 3 and 19. To date, no specific, fixed, or optimal values for them have yet been found that can be applicable to all situations. To find the optimal values for the three parameters, we first used coarse steps to obtain initial ranges, and then used fine steps to find the best values within the ranges. Segmented objects were visually inspected on its spectral homogeneity within image objects and heterogeneity among image objects. In general, the segmented objects would be more spectral homogeneous within image objects and heterogeneous among image objects. The reasonable results were from the middle scale and merge levels with small kernel sizes. The additional searches shown that a scale level of 50, a merge level of 50, and texture kernel size of 3 pixels, respectively, could be the best values for seagrass meadows in the Redfish Bay. Actually, the three parameters are not very sensitive to the specific values. For example, the scale level, merge level and the kernel size of 49, 51 and 5, respectively did not produce a big visual difference with the values of 50, 50 and 3.

ENVI Feature Extraction produced 266,565 polygons, namely segments, from nearly 8 million pixels in the study area. These segments have an average of 29 pixels from the minimal of 4 pixels to the maximal of 32,700 pixels.

3.2.3. Classification on Segmented Image Objects

We used the ISODATA algorithm to produce clusters of the above 266,565 segments. In total, there are 5 seagrass species in the Redfish Bay area [21]: *Halodule wrightii*, *Thalassia testudinum*, *Syringodium filiforme*, *Ruppia maritima* and *Halophila englemannii*. Two species, *Halodule wrightii* and *Thalassia testudinum*, co-dominate the seagrass assemblage. Here continuous meadow is an area with between 75–100% seagrass coverage of the substrate. Furthermore, no single seagrass specie has coverage more than 60% portion in the mixed meadow. Patchy meadow is area with between 10–75% bottom coverage by seagrass. Based on visual interpretation, we first combined the spectral classes produced by the ISODATA clustering into intermediate classes to obtain a smaller number of classes.

For example, 67 spectral classes were combined into 23 intermediate classes. Then based on in situ data, we assigned these intermediate classes to 5 categories of the seagrass classification. Specifically, an intermediate class is assigned majority species of seagrass. When no majority samples existed within an intermediate class, we assign a category for the class empirically. The in situ data consists of 219 samples collected during July 2008, which randomly distributed in Redfish bay shown in Figure 3 [69]. In the 5-class classification, the shallow-water benthic habitats were categorized into (1) continuous *Halodule wrightii* dominated meadow (*Halodule*), (2) continuous *Thalassia testudinum* dominated meadow (*Thalassia*), (3) continuous mixed seagrass meadow (mixed), (4) patchy seagrass meadow (patchy), and (5) bare substrate (bare). When the three continuous seagrass classes are combined, the 5-class classification is transformed to the 3-class classification in which the three categories are continuous and patchy seagrass and bare substrate.

3.2.4. Results and Accuracy Assessment

The classification results are shown with Figure 4. Accuracy of seagrass mapping were evaluated against the field survey data. The assessment data were from two sources: (1) 57 samples by field trips in September 2012, which located randomly in the study area (Figure 3); (2) 25 samples from 2011 field sampling of the Texas Seagrass Monitoring Plan [68]. The Texas Seagrass Monitoring Plan first tessellated the Redfish Bay by hexagons with 500 m sides, and then sampling locations were randomly selected within each polygon. There were 25 samples in the study area. Error matrixes [70] for the experiments were produced with both producer's and user's accuracy, and overall accuracy. Tables 3 and 4 are accuracy matrix for the 5-class and the 3-class classifications, respectively. Figure 4 displays the classification maps of both the 5-class and the 3-class classifications.

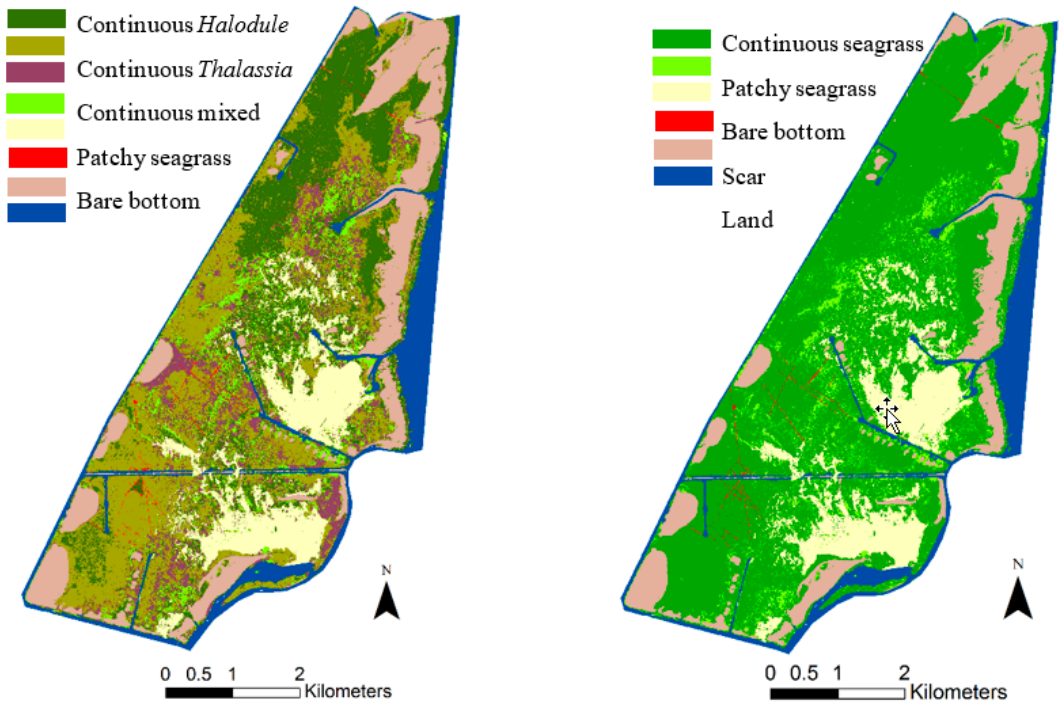

Figure 4. The 5-class map (**left**) and 3-class map (**right**) of seagrass in the Redfish Bay, Texas.

Table 3. Accuracy Matrix of the 5-class classification.

Class	*Thalassia*	*Halodule*	Mixed	Patchy	Bare	User's Accuracy
Thalassia	26	1	6	0	1	76%
Halodule	4	4	6	2	1	24%
Mixed	6	2	4	0	0	33%
Patchy	0	0	0	3	0	100%
Bare	1	0	0	0	15	94%
Producer's Accuracy	70%	57%	2 5%	60%	88%	63% (49.5%)

Table 4. Accuracy Matrix of the 3-class classification.

Class	Continuous	Patchy	Bare	User's Accuracy
Continuous	59	2	2	94%
Patchy	0	3	0	100%
Bare	1	0	15	94%
Producer's Accuracy	98%	60%	88%	94% (84.6%)

4. Discussion

Table 4 shows that seagrass can be effectively separated from bare bottom with high accuracy by the WorldView-2 imagery while the patchy was mislabeled the continuous seagrass by 2 out of 5 samples. Table 3 shows that species composition of seagrass cannot be efficiently identified by the approach. These results indicate that the high resolution satellite imagery is practical for mapping seagrass habitats (total accuracy 94% and kappa coefficient 84.6%) but not sufficient for identifying species composition (total accuracy 63% and kappa coefficient 49.5%).

Regarding remote sensing of benthic habitats, water column has strong effects on the remotely sensed reflectance of substrate cover types. However, not every investigator conducted water column correction. The water effects is two orders of magnitude stronger than the air. To reduce water column effects as much as possible, we carried out water column correction based on the bio-optical approach. The water column correction heavily depends on depth and spectral statistics of deep water sites, which show characteristics of the typical coastal water with chlorophyll and CDOM. In this study, the spectral statistics were similar but not exactly same in the five regions of interest (ROI) (Figure 1). ROI 2 and 4 were nearly identical due to both on the Gulf Intracoastal Waterway. ROI 1 had a little different spectral statistics from the others. Although ROI 1 is located outside of Redfish Bay, it still is included in this study because it close to several tidal inlets to the study area. Water would exchange regularly between the Bay and outside. In addition, the reflectance difference among the five ROIs is less than 1%. They are very similar in essential. Although using average of the five regions possibly leads to some places over-estimated and some places under-estimated, these distortions may not be too great. To show sensitivity of water-leaving reflectance to two key factors of the water column correction namely the reflectance of deep-water sites and depth, we conducted some simulations and the results are shown in Table 5. More specifically, at 0.25 m depth, 1 cm change of depth leads to 6.4 times or more changes of water-leaving reflectance than 1% reflectance change of deep-water sites. At 0.5 m depth, 1 cm change of depth leads to 3.6 times or more changes of water-leaving reflectance than 1% reflectance change of deep-water sites. The results show that the depth has primary effects. To some degree, the more accurate water depth, the better water column correction.

The benthic map typically provides depth from bottom. However, the seagrass meadows has canopy under water surface. We actually have two depths for the seagrass meadows. One is from the canopy, and another is the depth from the bottom. Figure 5 shows the depth distribution of the seagrass samples. There are two depths on each spot. The average depth from the bottom was 75 cm, and the average depth from the canopy was 39 cm. The water column correction in this study was on the depth from canopy. When seagrass meadow becomes sparser, coverage portion of substrate soil will go majority. The errors of the water column correction would be noteworthy. It would be helpful

that a water depth index directly derived from remote sensing imagery is used as an input feature of classification algorithms when the accurate depth measure is not available. Actually, Traganos et al. [8] used the depth invariant indices derived from Lyzenga's theory [48,71] to compensate the influence of variable depth on seabed habitats. Due to space, we do not discuss water column correction in details including deep water and the depth index directly derived from remote sensing imagery here.

Table 5. Spectral sensitivity at depth, reflectance change of deep water and depth change.

Variables		Spectral Responses			
Depth (m)	**Change**	**Blue**	**Green**	**Yellow**	**Red**
0.25	1% reflectance of deep water sites	0.00053	0.00045	0.00020	0.00015
	1 cm depth	0.0034	0.0031	0.0014	0.0010
	Ratio (depth: reflectance)	6.41	6.99	6.89	6.49
0.50	1% reflectance of deep water sites	0.00135	0.00111	0.00050	0.00040
	1 cm depth	0.0049	0.0045	0.0021	0.0015
	Ratio (depth: reflectance)	3.63	4.05	4.09	3.86

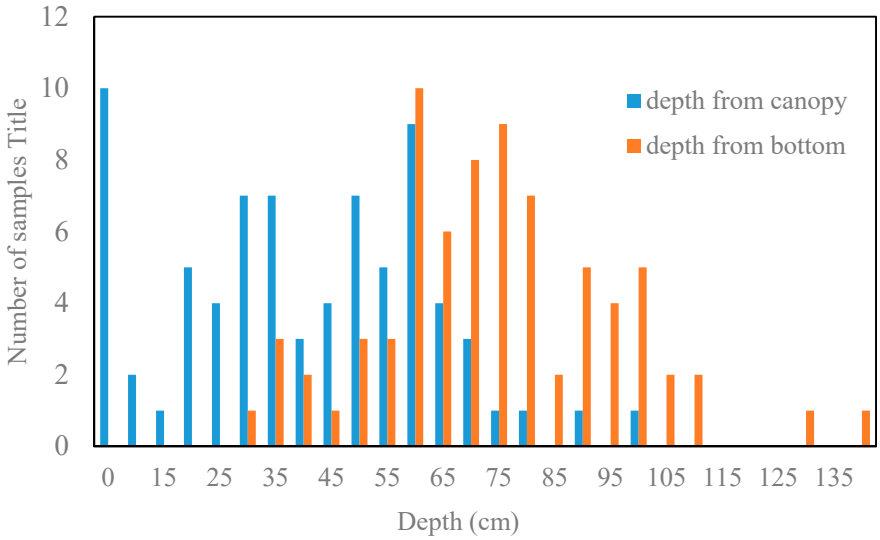

Figure 5. Depth distribution of samples (Red from bottom, blue from canopy).

Seagrasses support an extensive community of macro-algae and epiphytes [72]. The seagrass blades provide structure for the attachment and growth of epiphytic algae. The density of epiphytes increases toward the leaf tip and on the outermost [73]. The spectral response from seagrass blades can has substantial variation, depending on numerous factors including epiphyte coverage and the stage of senescence or morbidity [74,75]. The spotless, epiphyte-free seagrass blade is green. The epiphytes colonization changes color of seagrass blades from green at a low coverage to brown at high coverage. These facts reveal that the same seagrass species may have different spectral characteristics. Both upper photos on Figure 6 were taken in the study area on 30 August 2012. The upper left photo shows a lot of epiphyte on seagrass blades. The upper right photo on Figure 6 is a bunch of *Thalassia* blades and *Halodule* blades with epiphyte. Some blades are green and some are senescence. The bottom picture on Figure 6 shows the reflectance of clean *Thalassia* blade, *Thalassia* blade with epiphyte, *Halodule* blade with epiphyte, draft algae, and *Thalassia* canopy under 0.5 m water surface. Moreover, the submerged seagrass canopy is observed instead of individual epiphyte-covered blades by remote sensing instruments aboard aerial and space platforms. Another issue is the drift macro-algae that is ephemeral, drifting over the top and settling on the seagrass beds and in depressions such as scars [76]. Macro-algae accumulation in seagrass meadows changes the spectral signature of seagrass meadows. Differences in the spectra of the components within seagrass meadows possibly are not sufficient to explain the spectral variation of seagrass meadows, which consist of seagrass blades, drift algae, and

substrates. Thus, seagrass mapping may need the radiative transfer models of canopy to associate remote sensing observations with the spectra of the components. In addition, it would be favorable to collect seasonally the typical spectrum of seagrass and surrounding types (drift algae, epiphytes, detritus, etc.) due to their seasonal changes. As a result, we could regularly evaluate the water quality and ecological condition of the estuaries by identifying the temporal change of the spatial patterns of the seagrass distribution from the affordable high resolution imagery. Taking advantage of short revisit time of WorldView-2, we also can investigate the hurricane impacts to seagrass beds just after the hurricanes. Extreme wind events are becoming more frequent due to global climate change.

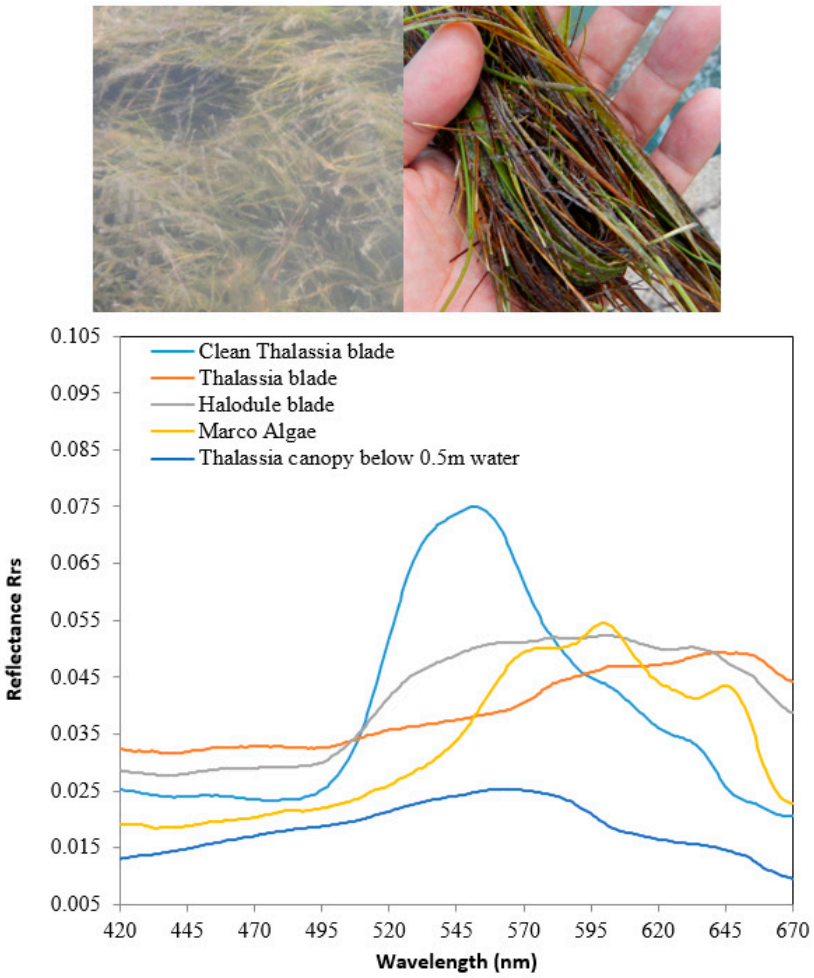

Figure 6. Reflectance of clean *Thalassia* blade, *Thalassia* blade with epiphyte, *Halodule* blade with epiphyte, draft algae, *Thalassia* canopy under 0.5 m water surface.

5. Conclusions

The classification experiments on the high spatial resolution satellite imagery demonstrate that it is practical to separate seagrass meadows from the bare bottom although the composition of seagrass species cannot be identified well. The OBIA is an effective approach to extracting features from imagery. The proposed water column correction based on the bio-optical approach is feasible when optically-deep water regions can be found on the image. The water depth indices directly derived from remote sensing imagery are necessary for seagrass mapping.

Author Contributions: Conceptualization, L.S. and Y.H.; methodology, L.S. and Y.H.; investigation, L.S. and Y.H.; writing, L.S. and Y.H.; funding acquisition, L.S.

Funding: This research was funded by the Texas Research Development and Research Enhancement Funds, grant number 140161.

Conflicts of Interest: The authors declare no conflict of interest.

References

1. Hemminga, M.A.; Duarte, C.M. *Seagrass Ecology*; Cambridge University Press: London, UK, 2000.
2. Orth, R.J.; Carruthers, T.J.B.; Dennison, W.C.; Duarte, C.M.; Fourqurean, J.W.; Heck, K.L.; Hughes, A.R.; Kendrick, G.A.; Kenworthy, W.J.; Olyarnik, S.; et al. A Global Crisis for Seagrass Ecosystems. *BioScience* **2006**, *56*, 987–996. [CrossRef]
3. Short, F.; Carruthers, T.; Dennison, W.; Waycott, M. Global seagrass distribution and diversity: A bioregional model. *J. Exp. Mar. Biol. Ecol.* **2007**, *350*, 3–20. [CrossRef]
4. Alongi, D.M. *Coastal Ecosystem Processes (Marine Science)*; CRC Press: Boca Raton, FL, USA, 1997.
5. Ferguson, R.L.; Wood, L.L.; Graham, D.B. Monitoring spatial change in seagrass habitat with aerial photography. *Photogramm. Eng. Remote Sens.* **1993**, *59*, 1033–1038.
6. Pasqualini, V.; Pergent-Martinia, C.; Pergenta, G.; Agreila, M.; Skoufasb, G.; Sourbesc, L.; Tsirikad, A. Use of SPOT 5 for mapping seagrasses: An application to Posidonia oceanica. *Remote Sens. Environ.* **2005**, *94*, 39–45. [CrossRef]
7. Dierssen, H.M.; Zimmerman, R.C.; Burdige, D.; Drake, L. Benthic ecology from space: Optics and net primary production in seagrass and benthic algae across the Great Bahama Bank. *Mar. Ecol. Prog. Ser.* **2010**, *411*, 1–15. [CrossRef]
8. Traganos, D.; Aggarwal, B.; Poursanidis, D.; Topouzelis, K.; Chrysoulakis, N.; Reinartz, P. Towards Global-Scale Seagrass Mapping and Monitoring Using Sentinel-2 on Google Earth Engine: The Case Study of the Aegean and Ionian Seas. *Remote Sens.* **2018**, *10*, 1227. [CrossRef]
9. Dierssen, H.M.; Zimmerman, R.C. Ocean color remote sensing of seagrass and bathymetry in the Bahamas Banks by high-resolution airborne imagery. *Limnol. Oceanogr.* **2003**, *48*, 444–455. [CrossRef]
10. Mobley, C.D.; Sundman, L.K.; Davis, C.O.; Bowles, J.H.; Downes, T.V.; Leathers, R.A.; Montes, M.J.; Bissett, W.P.; Kohler, D.D.R.; Reid, R.P.; et al. Interpretation of hyperspectral remote-sensing imagery by spectrum matching and look-up tables. *Appl. Opt.* **2005**, *44*, 3576–3592. [CrossRef] [PubMed]
11. Valle, M.; Pal, V.; Lafon, V.; Dehouck, A.; Garmendia, J.M.; Borja, A.; Chust, G. Mapping estuarine habitats using airborne hyperspectral imagery, with special focus on seagrass meadows. *Estuar. Coast. Shelf Sci.* **2015**, *164*, 433–442. [CrossRef]
12. Mishra, D.R.; Narumalani, S.; Rundquist, D.; Lawson, M. High-Resolution Ocean Color Remote Sensing of Benthic Habitats: A Case Study at the Roatan Island, Honduras. *IEEE Trans. Geosci. Remote Sens.* **2005**, *43*, 1592–1604. [CrossRef]
13. Green, K.; Lopez, C. Using Object-Oriented Classification of ADS40 Data to Map the Benthic Habitats of the State of Texas. *Photogramm. Eng. Remote Sens.* **2007**, *73*, 861–865.
14. Reshitnyk, L.; Costa, M.P.F.; Robinson, C.L.K.; Dearden, P. Evaluation of WorldView-2 and acoustic remote sensing for mapping benthic habitats in temperate coastal Pacific waters. *Remote Sens. Environ.* **2014**, *153*, 7–23. [CrossRef]
15. Eugenio, F.; Marcello, J.; Martin, J. High-Resolution Maps of Bathymetry and Benthic Habitats in Shallow-Water Environments Using Multispectral Remote Sensing Imagery. *IEEE Trans. Geosci. Remote Sens.* **2015**, *53*, 3539–3549. [CrossRef]
16. Koedsin, W.; Intararuang, W.; Ritchie, R.J.; Huete, A. An Integrated Field and Remote Sensing Method for Mapping Seagrass Species, Cover, and Biomass in Southern Thailand. *Remote Sens.* **2016**, *8*, 292. [CrossRef]
17. Duffy, J.P.; Pratt, L.; Anderson, K.; Land, P.E.; Shutler, J.D. Spatial assessment of intertidal seagrass meadows using optical imaging systems and a lightweight drone. *Estuar. Coast. Shelf Sci.* **2018**, *200*, 169–180. [CrossRef]
18. Zhao, D.; Jiang, H.; Yang, T.; Cai, Y.; Xu, D.; An, S. Remote sensing of aquatic vegetation distribution in Taihu Lake using an improved classification tree with modified thresholds. *J. Environ. Manag.* **2012**, *95*, 98–107. [CrossRef]
19. Hedley, J.D.; Russell, B.J.; Randolph, K.; Pérez-Castro, M.Á.; Vásquez-Elizondo, R.M.; Enríquez, S.; Dierssen, H.M. Remote Sensing of Seagrass Leaf Area Index and Species: The Capability of a Model Inversion Method Assessed by Sensitivity Analysis and Hyperspectral Data of Florida Bay. *Front. Mar. Sci.* **2017**, *4*, 362. [CrossRef]

20. Hossain, M.S.; Bujang, J.S.; Zakaria, M.H.; Hashim, M. The application of remote sensing to seagrass ecosystems: An overview and future research prospects. *Int. J. Remote Sens.* **2015**, *36*, 61–114. [CrossRef]
21. Pulich, W., Jr.; Blair, C.; White, W.A. *Current Status and Historical Trends of Seagrass in the Corpus Christi Bay National Estuary Program Study Area. Publication CCBNEP-20*; Texas Natural Resource Conservation Commission: Austin, TX, USA, 1997.
22. Blaschke, T. Object based image analysis for remote sensing. *ISPRS J. Photogram. Remote Sens.* **2010**, *65*, 2–16. [CrossRef]
23. Lillesand, T.M.; Kiefer, R.W.; Chipman, J.W. *Remote Sensing and Image Interpretation*, 6th ed.; John Wiley & Sons: Hoboken, NJ, USA, 2007.
24. Beyer, T.G.; Rasser, M.; Morehead, S. *Development of a Comprehensive Habitat Map for the Mission Aransas NERR Using the NERRS Habitat Classification Scheme: Matagorda Island, Texas*; Mission-Aransas National Estuarine Research Reserve: Aransas, TX, USA, 2007.
25. Asquith, W.H.; Mosier, J.G.; Bush, P.W. *Status, Trends and Changes in Freshwater Inflows to Bay Systems in the Corpus Christi Bay National Estuary Program Study Area. Publication CCBNEP-17*; Corpus Christi Bay National Estuary Program: Corpus Christi, TX, USA, 1997.
26. Fry, B.; Parker, P.L. Animal diet in Texas seagrass meadows: δ13C evidence for the importance of benthic plants. *Estuar. Coast. Mar. Sci.* **1979**, *8*, 499–509. [CrossRef]
27. Pulich, W., Jr. Chapter 1 Introduction. In *Seagrass Conservation Plan for Texas–1999*; Texas Parks and Wildlife: Austin, TX, USA, 1999.
28. U.S. Environmental Protection Agency (EPA). *The Ecological Condition of Estuaries in the Gulf of Mexico (EPA 620-R-98-004)*; U.S. Environmental Protection Agency: Washington, DC, USA, 1999.
29. Dunton, K.H. Seasonal growth and biomass of the subtropical seagrass Halodule wrightii in relation to continuous measurements of underwater irradiance. *Mar. Biol.* **1994**, *120*, 479–489. [CrossRef]
30. Burfeind, D.D.; Stunz, G.W. The effects of boat propeller scarring intensity on nekton abundance in subtropical seagrass meadows. *Mar. Biol.* **2006**, *148*, 953–962. [CrossRef]
31. Bukata, R.P.; Jerome, J.H.; Kondratyev, K.Y.; Pozdnyakov, D.V. *Optical Properties and Remote Sensing Inland Coastal Waters*; CRC Press: Boca Raton, FL, USA, 1995.
32. Martin, S. *An Introduction to Ocean Remote Sensing*; Cambridge University: London, UK, 2004.
33. Jensen, J.R. *Introductory Digital Image Processing*, 3rd ed.; Prentice-Hall: Upper Saddle River, NJ, USA, 2004.
34. Kay, S.; Hedley, J.D.; Lavender, S. Sun glint correction of high and low spatial resolution images of aquatic scene: A review of methods for visible and near-infrared wavelengths. *Remote Sens.* **2009**, *1*, 697–730. [CrossRef]
35. Hochberg, E.; Andrefout, S.; Tyler, M. Sea surface correction of high spatial resolution Ikonos images to improve bottom mapping in near-shore environments. *IEEE Trans. Geosci. Remote Sens.* **2003**, *41*, 1724–1729. [CrossRef]
36. Hedley, J.; Harborne, A.; Mumby, P. Simple and robust removal of sun glint for mapping shallow-water benthos. *Int. J. Remote Sens.* **2005**, *26*, 2107–2112. [CrossRef]
37. Lyzenga, D.R. Shallow-water bathymetry using combined lidar and passive multispectral scanner data. *Int. J. Remote Sens.* **1985**, *6*, 115–125. [CrossRef]
38. Mobley, C.D. *Light and Water: Radiative Transfer in Natural Waters*; Academic Press: New York, NY, USA, 1994.
39. Stumpf, R.P.; Pennock, J.R. Calibration of a general optical equation for remote sensing of suspended sediments in a moderately turbid estuary. *J. Geophys. Res.* **1989**, *94*, 14363–14371. [CrossRef]
40. Stumpf, R.P.; Holderied, K. Determination of water depth with high-resolution satellite imagery over variable bottom types. *Limnol. Oceanogr.* **2003**, *48*, 547–556. [CrossRef]
41. Evans, R.H.; Gordon, H.R. Coastal zone color scanner 'system calibration': A retrospective examination. *J. Geophys. Res.* **1994**, *99*, 7293–7307. [CrossRef]
42. Elterman, L. *UV, Visible, and IR Attenuation for Altitudes to 50 km*; AFCRL-68-0153, Environmental Research Papers, No. 285; Air Force Cambridge Research Laboratories: Bedford, MA, USA, 1968.
43. Updike, T.; Comp, C. Radiometric Use of WorldView-2 Imagery, Technical Note, DigitalGlobe, 1 November 2010. Available online: https://dg-cms-uploads-production.s3.amazonaws.com/uploads/document/file/104/Radiometric_Use_of_WorldView-2_Imagery.pdf (accessed on 6 April 2019).
44. Lyzenga, D.R.; Malinas, N.P.; Tanis, F.J. Multispectral Bathymetry Using a Simple Physically Based Algorithm. *IEEE Trans. Geosci. Remote Sens.* **2006**, *44*, 2251–2259. [CrossRef]

45. Philpot, W.D. Bathymetric mapping with passive multispectral imagery. *Appl. Opt.* **1989**, *28*, 1569–1578. [CrossRef]
46. Ji, W.; Civco, D.L.; Kennard, W.C. Satellite remote bathymetry: A new mechanisms for modeling. *Photogram. Eng. Remote Sens.* **1992**, *58*, 545–549.
47. Mumby, P.J.; Green, E.P.; Edwards, A.J.; Clark, C.D. Measurement of seagrass standing crop using satellite and digital airborne remote sensing. *Mar. Ecol. Prog. Ser.* **1997**, *159*, 51–60. [CrossRef]
48. Lyzenga, D.R. Remote sensing of bottom reflectance and water attenuation parameters in shallow water using aircraft and Landsat data. *Int. J. Remote Sens.* **1981**, *2*, 71–82. [CrossRef]
49. Lafon, V.; Froidefond, J.M.; Lahet, F.; Castaing, P. SPOT shallow water bathymetry of a moderately turbid tidal inlet based on field measurements. *Remote Sens. Environ.* **2002**, *81*, 136–148. [CrossRef]
50. Schweizer, D.; Armstrong, R.A.; Posada, J. Remote sensing characterization of benthic habitats and submerged vegetation biomass in Los Roques Archpelago National Park, Venezuela. *Int. J. Remote Sens.* **2005**, *26*, 2657–2667. [CrossRef]
51. Mertes, L.A.K.; Dekker, A.G.; Brakenridge, G.R.; Birkett, C.M.; Letourneau, G. Rivers and Lakes. In *Remote Sensing for Natural Resource Management and Environmental Monitoring*; Ustin, S.L., Ed.; John Wiley and Sons: New York, NY, USA, 2004; pp. 345–400.
52. Davis, C.O.; Lamela, G.M.; Donato, T.F.; Bachmann, C.M. Coastal Margins and Estuaries. In *Remote Sensing for Natural Resource Management and Environmental Monitoring*; Ustin, S.L., Ed.; John Wiley and Sons: New York, NY, USA, 2004; pp. 401–446.
53. Richardson, L.L.; LeDrew, E.F. Remote Sensing and the Science, Monitoring, and Management of Aquatic Coastal Ecosystems. In *Remote Sensing of Aquatic Coastal Ecosystem Processes: Science and Management Applications*; Richardson, L.L., LeDrew, E.F., Eds.; Springer: Dordrecht, The Netherlands, 2006; pp. 1–7.
54. Zaneveld, J.R.V.; Twardowski, M.J.; Barnard, A.; Lewis, M.R. Introduction to radiative transfer. In *Remote Sensing of Coastal Aquatic Environments: Technologies, Techniques and Applications*; Miller, R.L., Del Castillo, C.E., McKee, B.A., Eds.; Springer: Dordrecht, The Netherlands, 2005; pp. 1–20.
55. Lee, Z.P.; Carder, K.L. Hyperspectral Remote Sensing. In *Remote Sensing of Coastal Aquatic Environments: Technologies, Techniques and Applications*; Miller, R.L., Del Castillo, C.E., McKee, B.A., Eds.; Springer: Dordrecht, The Netherlands, 2007; pp. 181–204.
56. Lee, Z.P.; Carder, K.L.; Mobley, C.D.; Steward, R.G.; Patch, J.S. Hyperspectral remote sensing for shallow waters: 2. Deriving bottom depths and water properties by optimization. *Appl. Opt.* **1999**, *38*, 3831–3843. [CrossRef]
57. Lee, Z.P.; Carder, K.L.; Mobley, C.D.; Steward, R.G.; Patch, J.S. Hyperspectral remote sensing for shallow waters. 1. A semianalytical model. *Appl. Opt.* **1998**, *37*, 6329–6338. [CrossRef]
58. Austin, R.W.; Petzold, T.J. Spectral dependence of diffuse attenuation coefficient of light in ocean waters. *Opt. Eng.* **1986**, *25*, 471–479. [CrossRef]
59. Morel, A. Optical modeling of the upper ocean in relation to its biogenous matter content (case 1 waters). *J. Geophys. Res.* **1988**, *93*, 10749–10768. [CrossRef]
60. Pope, R.M.; Fry, E.S. Absorption spectrum (380–700 nm) of pure water. II. integrating cavity measurements. *Appl. Opt.* **1997**, *36*, 8710–8723. [CrossRef]
61. Lee, Z.P.; Carder, K.L.; Steward, R.G.; Peacock, T.G.; Davis, C.O.; Patch, J.S. An empirical algorithm for light absorption by ocean water based on color. *J. Geophys. Res.* **1998**, *103*, 27967–27978. [CrossRef]
62. Morel, A.; Gentili, B. Diffuse reflectance of oceanic waters: Its dependence on sun angle as influenced by the molecular scattering contribution. *Appl. Opt.* **1991**, *30*, 4427–4438. [CrossRef]
63. Smith, R.C.; Baker, K.S. Optical properties of the clearest natural waters (200–800 nm). *Appl. Opt.* **1981**, *20*, 177–184. [CrossRef]
64. Gordon, H.R.; Smith, R.C.; Zaneveld, J.R.V. Introduction to ocean optics. *Proc. SPIE* **1980**, *208*, 1–43.
65. Sathyendranath, S.; Prieur, L.; Morel, A. A three-component model of ocean colour and its application to remote sensing of phytoplankton pigments in coastal waters. *Int. J. Remote Sens.* **1989**, *10*, 1373–1394. [CrossRef]
66. Lee, Z.P.; Darecki, M.; Carder, K.L.; Davis, C.O.; Stramski, D.; Rhea, W.J. Diffuse attenuation coefficient of downwelling irradiance: An evaluation of remote sensing methods. *J. Geophys. Res.* **2005**, *110*, C02017. [CrossRef]

67. Morel, A.; Gentili, B. Diffuse reflectance of oceanic waters II. Bi-directional aspects. *Appl. Opt.* **1993**, *32*, 6864–6879. [CrossRef]
68. Wilson, C.J.; Dunton, K.H. *Assessment of Seagrass Habitat Quality and Plant Physiological Condition in Texas Coastal Waters*; The University of Texas at Austin Marine Science Institute: Port Aransas, TX, USA, 2012.
69. Wood, J.S. Hyperspectral Analysis of Seagrass in Redfish Bay, Texas. Ph.D. Dissertation, Texas A&M University-Corpus Christi, Corpus Christi, TX, USA, 2012.
70. Congalton, R.G.; Green, K. *Assessing the Accuracy of Remotely Sensed Data: Principles and Practices*, 2nd ed.; CRC Press: Boca Raton, FL, USA, 2009.
71. Lyzenga, D.R. Passive remote sensing techniques for mapping water depth and bottom features. *Appl. Opt.* **1978**, *17*, 379–383. [CrossRef]
72. Mann, K.H. *Ecology of Coastal Waters with Implication for Management*, 2nd ed.; Blackwall Science: Malden, MA, USA, 2000.
73. Borowitzka, M.A.; Lethbridge, R.C. Seagrass epiphytes. In *Biology of Seagrasses, Aquatic Plant Studies*; Larkum, A.W.D., McComb, A.J., Shepard, S.A., Eds.; Elsevier: New York, NY, USA, 1989; pp. 458–499.
74. Fyfe, S.K. Spatial and temporal variation in spectral reflectance: Are seagrass species spectrally distinct? *Limnol. Oceanogr.* **2003**, *48*, 464–479. [CrossRef]
75. Thorhaug, A.; Richardson, A.D.; Berlyn, G.P. Spectral reflectance of the seagrasses: Thalassia testudinum, Halodule wrightii, Syringodium filiforme and five marine algae. *Int. J. Remote Sens.* **2007**, *28*, 1487–1501. [CrossRef]
76. Cowper, S.W. The drift algae community of seagrass beds in Redfish Bay, Texas. *Contrib. Mar. Sci.* **1978**, *21*, 125–132.